Highly-repeatable generation of very small nanoparticles by Pulsed-Laser Ablation in Liquids of a high-speed rotating target

Amandine Resano-Garcia, Stéphane Champmartin, Yann Battie, Alain Koch, Aotmane En Naciri, Abdelhak Ambari, Nouari Chaoui

Highly-repeatable generation of very small nanoparticles by Pulsed-Laser Ablation in Liquids of a high-speed rotating target

A. Resano-Garcia[a], S. Champmartin[b], Y. Battie[a], A. Koch[a], A. En Naciri[a], A. Ambari[b] and N. Chaoui[a,*]

[a] LCP-A2MC, Institut Jean Barriol, Université de Lorraine, 1, Bd Arago, 57070 Metz, France

[b] LAMPA, ENSAM d'Angers, 2, Bd du Ronceray, BP 93525, 49035 Angers, France

Keywords : Laser ablation ; Nanoparticles ; Colloids ; Optical properties; Catalysis

Abstract

By irradiating a cylindrical silver target rotated at high-speed within the range 300 – 2400 rpm (lateral speed 0.16 – 1.25 $m.s^{-1}$) in *pure water*, we prepare ligand-free Ag nanoparticles (NPs) with size of 4±2 nm which are likely to be primary particles. Usually, the generation of NPs showing such a small size requires either a laser post–treatment and/or chemical additives. As the rotation rate of the target is increased, calculated 3D flow patterns revealed different hydrodynamic regimes which clearly influence the ablation rate and repeatability of the process as well as the colloids properties. In addition to revealing the importance of fluid dynamics in Pulsed-Laser Ablations in Liquids, this study provides a way for producing in one step *pure* NPs with size below 5 nm which are suitable for applications in catalysis.

*Corresponding author: nouari.chaoui@univ-lorraine.fr

Introduction

In its principle, Pulsed-Laser Ablation in Liquids[1,2,3,4](PLAL) appears as simple and versatile method to produce ligand-free nanoparticles[2,3,4] which found applications in areas such as biomedicine[5,6], bio-sensing[7,8] and catalysis[9,10]. However, due to the numerous processing parameters and their complex interdependence, this method has the main disadvantages of i) presenting a lack of particle size control ii) having a relatively weak productivity[2,3,4] iii) being hardly reproducible[2]. The complexity of PLAL is well-illustrated by the progressive attenuation of the laser beam by the colloids during the ablation. When performed in a steady solution, the mechanisms responsible for the particles transport are mainly diffusion (Brownian motion) and free convection due to changes in liquid density[11]. Because these processes are slow, particles accumulate in front of the target due to the multi-pulses ablation explaining this attenuation of the laser beam. This attenuation of the laser beam has consequences on the nanoparticles size /shape distributions and the ablation rate.

Tsuji et al[12] studied the effect of wavelength on the ns-laser ablation rate of a silver target in water on the resulting particle size. They observed a decrease of the mean particle diameter from 29 to 12 nm and of the ablation rate with decreasing laser wavelength. They explained these results by the wavelength dependence of the absorption of the laser beam by the colloids. During ns-pulsed irradiation of silver at 1064 nm in water, Prochazka et al.[13] observed a decrease of the mean diameter of nanoparticles down to 12 nm as the number of pulses was increased. Further decrease of the size of Ag NPs, below 10 nm, using ns-laser pulses requires the use of ligands as shown by Mafuné et al. [14]. Recently, we also showed the impact of this attenuation of the laser beam on the shape distribution of the nanoparticles[15].

Regarding ablation rate and relative productivity, it is still difficult to find clear information about silver colloids. In conventional batch system, the ablated amount of silver is usually evaluated from the extinction value at 250 nm in the interband region of the spectra which not

affected by the size and shape of the NPs[12,14,14,16,17]. Using ns-laser pulses at 1064 nm for preparing silver colloid by PLAL, Mafuné et al.[14] estimate an ablation rate of the order of 2.10^{-4} mg/pulse which corresponds, in their experimental conditions, to a relative productivity (mass/processing time/laser power) of about 1 mg/Wh.

The effect of forced convection during ns-laser ablation in liquid has been examined by several authors who found that the ablation rate of the experiment were significantly improved[**Erreur ! Signet non défini.**,17,17]showing again the importance of the particles transport in the PLAL process. The productivity is further improved by using liquid flow-based systems. By performing ps-laser pulse ablation of silver at 1064 nm in a closed-loop liquid flow cell, Barcikowski et al[18] achieved a maximum relative productivity of 5.6 mg/Wh. R. Streubel et al.[19] demonstrated the possibility to generate Ag colloids with absolute productivity of 1.8 g/h (measured after one hour ablation) in a liquid flow cell. They used ultra-high repetition rate laser (1030 nm, 3 ps, 10.1 MHz) that was scanned on the target surface at high speed (500 $m.s^{-1}$). In addition to renew the surface under the laser flux to avoid excessive digging, scanning the target at high-speed aims to bypass the cavitation bubble which is the major issue encountered at high repetition rate.[19,19] In this system, the particle transport is performed by the liquid flowing along the target surface using a circulating pump with limited flow velocity in order to ensure sufficiently concentrated colloids.

In this work, we adopt an alternative and complementary strategy in which the laser beam is stationary and the target surface is set in motion at high-speed. We propose a novel design of PLAL setup, based on the irradiation of cylindrical target rotated at high-speed in analogy with the principle of the rotating cylinder electrode[20]. There is a fundamental difference between scanning a target surface using a galvanometer and setting in motion the target surface. In addition to renewing the surface exposed to the laser flux, the rotation of the target drives fluid flow and a shear stress in the vicinity of the surface. This should promote efficient

nanoparticles transport from the surface of the bulk and reduce the screening effect of the generated particles as the laser proceeds. We investigate the effect of the rotation rate of the target on the fluid dynamics and nanoparticles mass transport and their impacts on the properties (size and shape) of the produced colloids, the ablation rate and the repeatability of the process.

Experimental section

The PLAL experiments (Fig.1) were carried out using the fundamental wavelength (1064 nm) of a Nd-YAG laser (Continuum Surelite I-10) with a pulse duration of 6 ns and operated in all experiments at a repetition rate of 10 Hz. A $\lambda/2$ plate in combination with a thin polarizer was used as an extracavity attenuator in order to allow a precise adjustment of the laser energy and to ensure, at the same time, a good pulse-to-pulse stability (< 2%).

A 10 mm-long and 1 mm-thick silver tube (Aldrich, 99.99 % purity) with external diameter of 10 mm was used as a target. It was press fitted on a rod with 8 mm diameter that was attached to a DC brushless motor (BLDC 58, McLennan). The target was immersed in a 40 mm-light path borosilicate cell filled with 20 ml of ultra-pure water (18 MΩ.cm). The rotation rate of the target was varied within the range 300 – 2400 rpm. Table 1 presents the lateral speed, the Reynolds number and the lateral interpulse distance at 10 Hz for several values of rotation rate. The lateral speed of the target reaches 1.25 $m.s^{-1}$ which is comparable to the scan velocities of galvanometer scanners[21].

Table 1: Lateral speed, Reynolds number and lateral interpulse distance for several rotation rates of the target (in rpm and Hz)

Rotation rate (rpm)	Rotation rate (Hz)	Lateral speed ($m.s^{-1}$)	Reynolds number	Lateral interpulses distance at 10 Hz (cm)
300	5	0.16	1571	1.6

1200	20	0.62	6284	6.2
2400	40	1.25	12570	12.5

The laser beam was focused on the target surface (spot diameter: 600 µm) through the entrance face of the cell by means of a plano-convex borosilicate lens of 30 mm focal length. In all experiments, the target was exposed to the laser beam during 300s at a laser fluence of 10 J/cm^2 (30 mJ/pulse).

In order to avoid excessive laser flux on the focusing lens and the entrance face of the cell, a beam expander (x2) has been placed before the focusing lens. The distance covered by the laser beam in the water was 12 mm.

Before each experiment, the silver target was polished with a 4000 micromesh sand paper to achieve a smooth surface. The target was then successively cleaned in ultrasonic baths with acetone, isopropanol and deionized water (10 min. each).

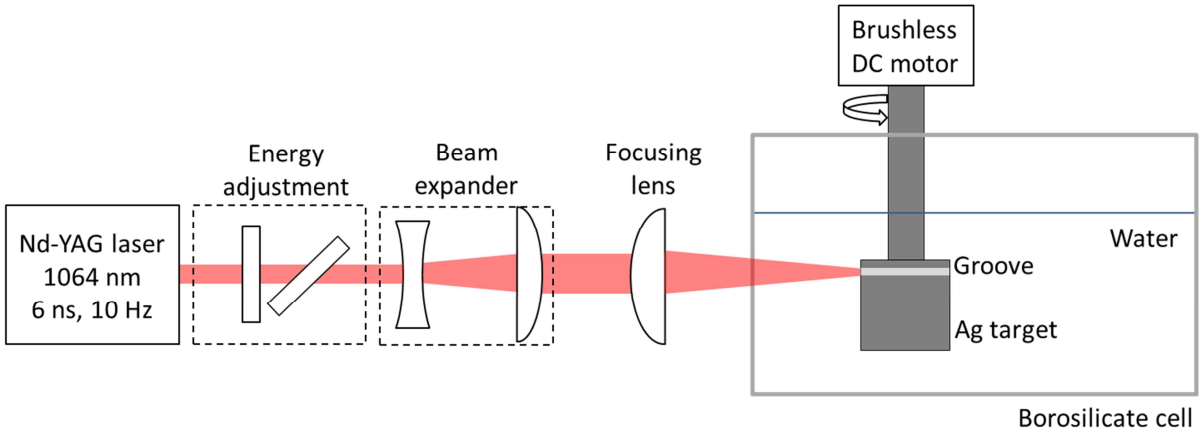

Figure 1: Schematic diagram of the experimental setup used to produce the Ag colloids.

The size distribution of the particles was measured by means of a Transmission Electron Microscopy (JEOL JEM-200S) operated at 100 kV. Just after each experiment, a drop of the as-prepared colloids was deposited on a copper grid and dried in air. The extinction spectra of

the generated colloids were recorded on a UV-visible spectrophotometer (Libra S12, Biochrom).

We use ANSYS Fluent (CFD) software to obtain the numerical solutions of the flow patterns. It is based on the finite-volume discretization method to evaluate the governing equations in the form of algebraic equations. In our simulations, the physical properties of water are taken constant ($\mu = 10^{-3}\ Pa.s$ and $\rho = 10^{3} kg/m^{3}$). According to Gabe and Walsh[20], the flow around a rotating cylinder is fully turbulent for $Re = \rho\omega d^{2}/2\mu\ > 100$. Using the target diameter $d = 10\ mm$ and its angular speed $\omega = 2\pi f$, the Reynolds number in our simulations is within the range 1571-12570 (table 1) and we use the standard $k - \varepsilon$ turbulence model. Likewise in these regimes, the flows are possibly unsteady and the time step is taken as $\Delta t = 1/(100f)$ in order to accurately capture the time-dependent phenomena. For each frequency f, we perform a grid convergence study on a structured HOH mesh topology. A special care is taken for the grid close to the target where the velocity gradients are the largest and the centrifugal hydrodynamic instabilities are likely to occur. To accelerate the computation, the deformation of the free surface close to the spinning target is neglected and a zero shear stress boundary condition is imposed on this horizontal free surface.

Results

Figure 2 compares a set of six extinction spectra of colloidal solutions prepared at low (300 rpm, Fig. 2 (a)) and high rotation rate (2400 rpm, Fig.2 (b)). At low rotation rate the extinction spectra (Fig.2 (a)) are very similar suggesting a high degree of repeatability of the experiments. The maximum of the surface plasmon resonance (SPR) band is localized at λ_{max}=395 nm and the plasmon band intensity is around 1. By contrast, the extinction spectra of colloidal solutions prepared at high rotation rate are much less repeatable (Fig. 2 (b)).

We have recently shown[Erreur ! Signet non défini.] that the width of laser-machined groove on the target reflects the attenuation of the laser energy by the generated particles which accumulate in front of the target (in the hydrodynamic boundary layer) during the process. Therefore, they were systematically examined after each experiment set. Fig. 2 present a photograph of the 6 grooves left by the laser on the target rotated at 300 rpm (Fig.2 (c)) and 2400 rpm (Fig.2 (d)). At low rotation rate, the grooves present sharp edges and their widths are highly repeatable whereas at high rotation rate, except for the two firsts, they are irregular, narrower and a close inspection of the image (inlet in Fig. 2(d)) shows that some of them present wavy edges. These results also reveal a clear correlation between the repeatability of the groove width and the repeatability of the colloids properties as appreciated from the extinction spectra.

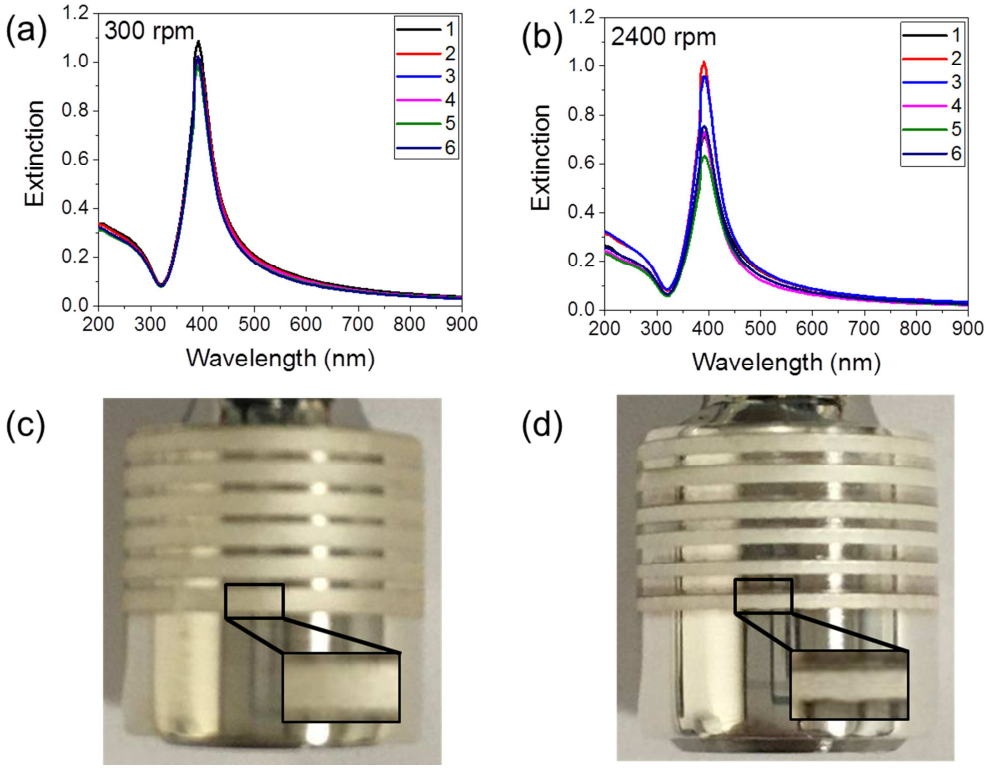

Figure 2: Set of 6 extinction spectra of silver colloidal solutions prepared at a rotation rate of (a) 300 rpm and (b) 2400 rpm and the resulting laser-machined grooves on the target rotated at (c) 300 rpm and (d) 2400 rpm.

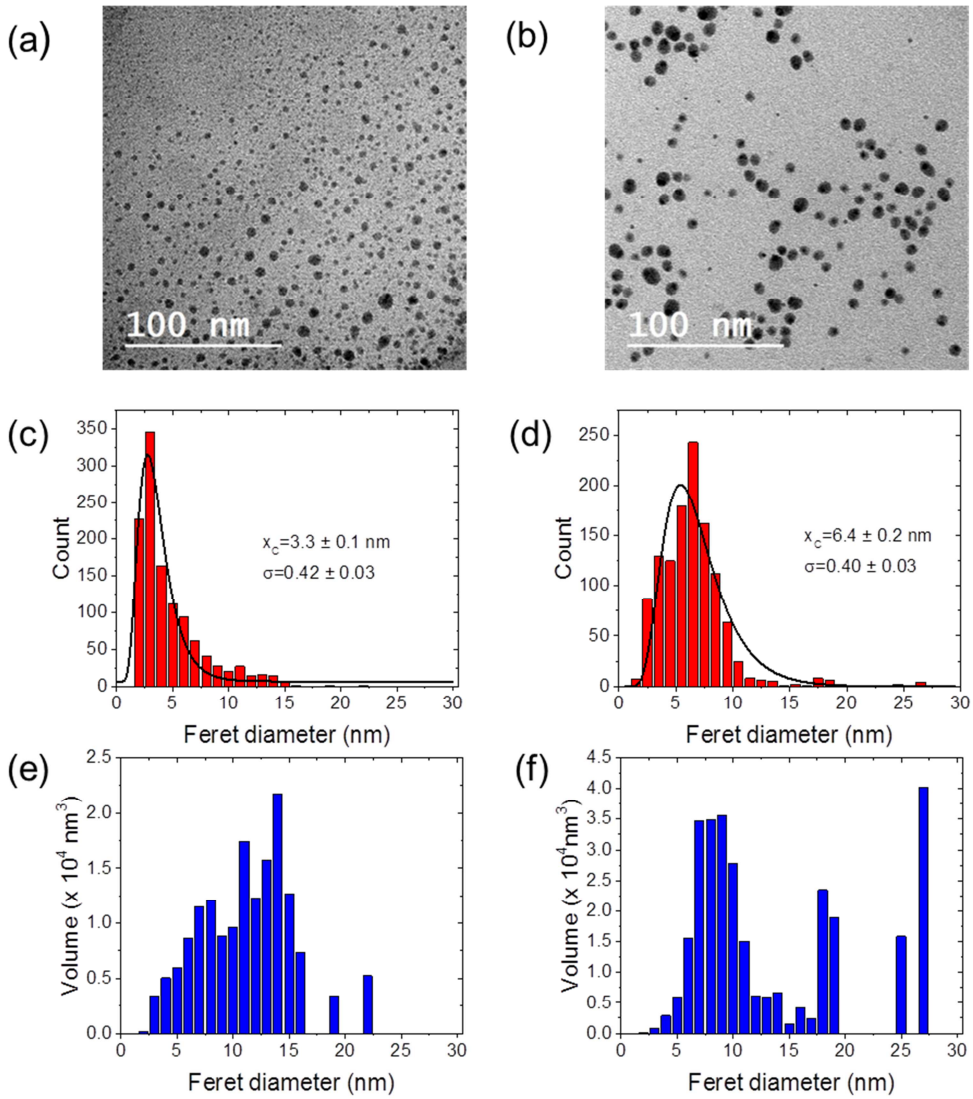

Figure 3: Representative TEM micrographs (a, b), number-weighted size distribution with lognormal fits (c, d) and volume-weighted size distribution (e, f) of the particles generated at a rotation rate of 300 rpm (left column) and 2400 rpm (right column). The number of counted particles was in both cases of about 1200.

The TEM micrographs (Fig. 3(a),(b)) of the particles agree well with the general aspect of the extinction spectra. For low and high rotation rate, the number-weighted size distribution of the nanoparticles is well-described by a monomodal lognormal law. At low rotation rate very small and spherical particles with mean size of 3.3 nm can be obtained in pure water while at high rotation rate the mean size of the particles is twice larger. Furthermore, in this latter case,

nanoparticles with Feret diameter larger than 15 nm are more frequent as seen from the representative TEM images (Fig. 3(b)) and the number-weighted distribution (Fig. 3(d)). While number-weighted size distribution shows a monomodal distribution, the volume-weighted size distributions (Fig. 3 (e), (f)) clearly shows a bimodal distribution. The first mode is centred around 8-10 nm while the second one is in the range 15-30 nm. Note that the second mode is more intense for the particles generated at high rotation rate (Fig. 3(f)). This difference between number- and volume-weighted distributions has been previously reported by Marzun et al.[22] for palladium colloids prepared by PLAL with ps-laser pulses.

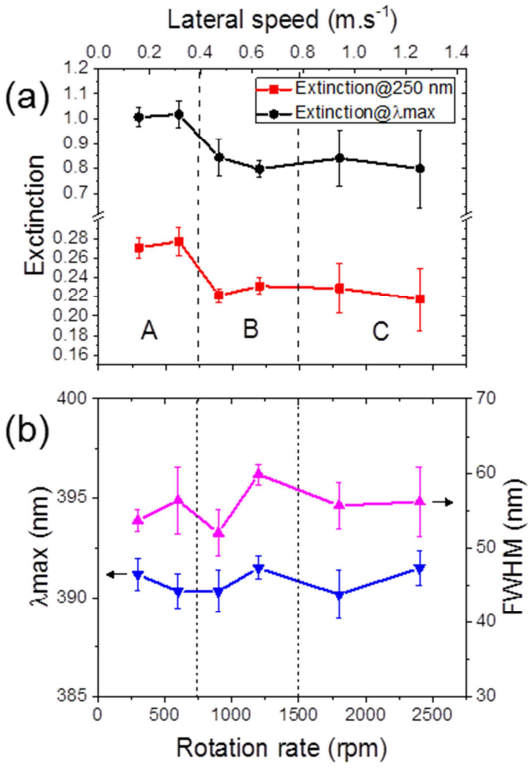

Figure 4: (a) Extinction at 250 nm and plasmon band intensity and (b) Full-width at half maximum and position of the plasmon band (λmax) as a function of the rotation rate of the target. The error bars represent the standard deviation calculated for a set of 6 samples.

The main characteristics of the extinction spectra are considerably affected by the concentration, size, shape and aggregation level of the NPs. Therefore, UV-visible

spectroscopy can also provide information on the particles population[14,16]. The extinction at 250 nm which is related to the amount of ablated material[14,16] and the plasmon band intensity are presented in Fig. 4(a). Both curves drop abruptly around 750 rpm and otherwise remain almost unchanged as the rotation speed of the target increases. The amount of ablated silver and the plasmon band intensity were on average reduced by about 20 %. Above approximately 1500 rpm, the repeatability of the process markedly decreases as seen from the increase uncertainty bars in Fig. 4(a). These trends reveal three different rotation rate regimes which we have called regimes A, B and C. In regime A (low rotation rate), the particles are produced with the highest production yield and a high repeatability while in regime B, the production yield decreases by 20 % without consequences on the repeatability which remains unchanged. In regime C, both repeatability and production yield appear clearly degraded. By contrast, the FWHM and the position of the plasmon band (Fig. 4(b)) do not show significant dependence on the rotation rate. This is consistent with the fact that the particles size and shape are poorly affected by the rotation rate of the target.

Since all the parameters were kept constant except for the rotation rate, the different regimes described in Fig. 4 are likely to be related to changes in the liquid flow as the rotation rate is tuned. Figure 5 shows the results of the numerical simulations of the 3D flows calculated at 300 (regime A), 1200 (regime B) and 2400 rpm (regime C) in front of the target. As the rotation rate is increased, the flow patterns in the bulk solution and in the vicinity of the target exhibit significant modifications. As our system is akin to a Taylor-Couette device, we can suspect that the flows in our simulations are prone to the same centrifugal instability, leading to the various flow patterns numerically obtained.

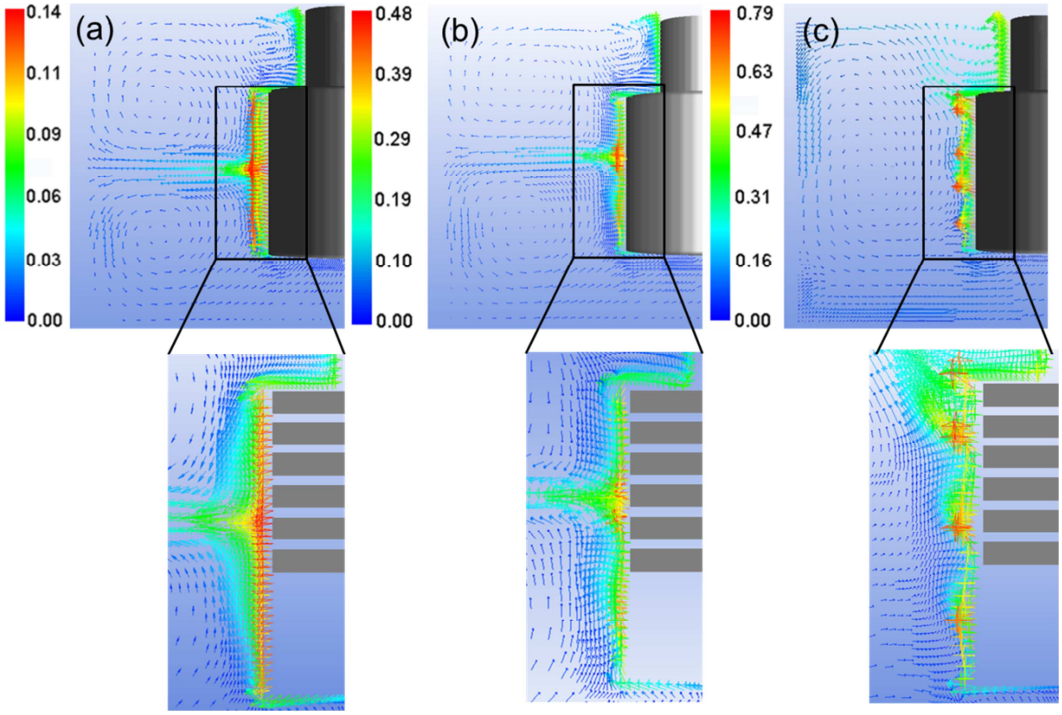

Figure 5: Velocity fields calculated for a rotation rate of (a) 300 rpm (regime A), (b) 1200 rpm (regime B) and (c) 2400 rpm (regime C). The colour scales represent the velocity module in $m.s^{-1}$. The bottom panels present a magnification of the region close to the target surface. The positions of the laser-machined grooves on the target have been indicated as grey rectangles as guide for the eyes.

At 300 rpm (Fig. 5(a)), the part of the solution nearer the target surface tends to rotate with the target with a quite smooth and simple profile. In the bulk, due to the centrifugal forces, the flow is mainly composed of two large superposed and steady counter-rotating toroidal vortices that meet in the horizontal mid-plane of the target, generating a high velocity zone in this plane. Between the base of the target and the bottom of the cell, two smaller vortices appear which are related to a von Kármán layer[23,24] (flow induced by a rotating disk). Similar flow patterns were obtained for the calculation performed at 600 rpm (not presented here). As the rotation rate is increased, the flow patterns become more and more complex. At 1200 rpm (Fig. 5(b)), in the bulk solution, the large vortex in the lower part of the cell grows and

the upper one shifts upward and shrinks. The flow field close to the target becomes less uniform and new flow patterns start to develop. The significant changing in the flow field is the typical feature of a hydrodynamic bifurcation. As the rotation rate is further increased (2400 rpm, Fig. 5(c)), the flow becomes space and time-dependent and four small unsteady vortices appear close to the target (Fig. 5(c)).

These modifications in flow regime have direct consequences on the torque exerted by the fluid on the rotating target. Its evolution as a function of time is presented for different values of the rotation rates (Fig. 6). At low rotation rates, the torque quickly reaches a steady value. For increasing values of the rotation rate, the appearance of the unsteady flow seen in Fig. 5(b) coincides with the onset of a time dependence of the torque. This is clearly apparent at 2400 rpm where the torque fluctuates randomly with time.

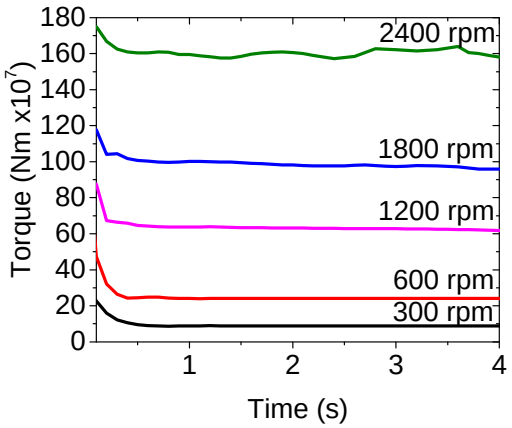

Figure 6: Time evolution of the torque exerted by the fluid on the target for several rotation rates.

In Fig.7 we have plotted the velocity module along two particular lines. In Fig. 7 (a), the curves are plotted along the x-direction at a constant altitude z=1.3 cm above the bottom of the cell (radial distribution of the velocity module). The curves at 300 rpm and 1200 rpm are

quite similar in shape (evidently at 1200 rpm greater velocities are found) but the flow disturbance due to the fluid motion in the radial direction extends little and rapidly decays. The curve at 2400 rpm is markedly different. The flow field disturbance extends further radially evidencing a change in the hydrodynamic regime and the manifestation of the toroidal vortices stacked one on top of the other along the target. In order to better highlight this phenomenon, we have also plotted the velocity module in another direction (Fig. 7(b)). The curves are plotted along the z-direction at a constant x position x=-0.1 cm to the left of the target (axial distribution of the velocity module). At 300 rpm, the profile is almost symmetrical with respect to the midplane z=1 cm with no vortices. At 2400 rpm, the vortices are now clearly visible. At the intermediate rotation rate 1200 rpm the hydrodynamic instability is not fully developed yet (transitional regime).

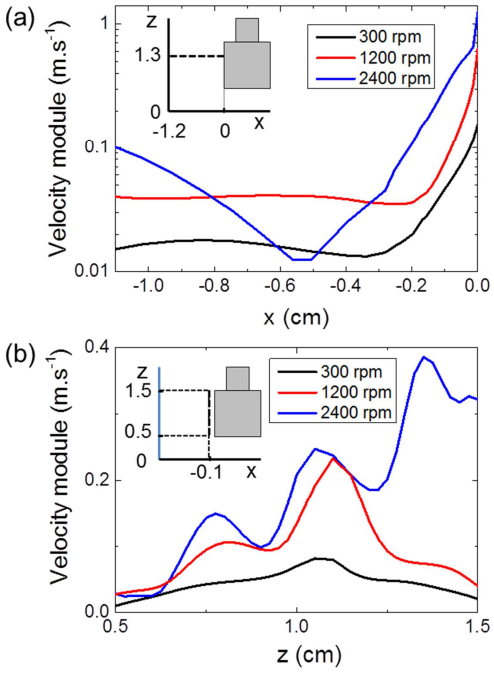

Figure 7: (a) Horizontal profile at constant altitude z=1.3 cm (z=0 at the bottom of the cell) of the velocity module as a function of distance x from the target (x=0 at the target surface). (b) Vertical profile of the velocity module at a constant distance x=-0.1 cm along the target

surface between z=0.5 and z=1.5 cm. The insets represent the relative position of the target and the edges of the cell.

Discussion

The flow patterns (Fig. 5) and the three different regimes described in Fig. 4 appear to be closely related. In regime A, the hydrodynamic boundary layer is quite simple and can clearly be correlated to the repeatability of the process as well as that of the laser-machined groove characteristics on the target (Fig. 2(c)). The flows are mainly azimuthal (except in the mid-plane) and steady along the target explaining the high repeatability of the process. The particles are efficiently taken away from the target and mixed in the bulk solution. In regime C, the flow patterns were found to be markedly different. In the vicinity of the target, the flow is characterized by four small toroidal vortices which are space and time-dependent. The lack of repeatability of the process and the lower production yield at this flow regime is consistent with the onset of such instabilities. The regime B corresponds to a transitional regime (bifurcation) where the large cells are unstable and start to deform.

The transient nature in regime C of these flow patterns might also rationalize the characteristics of the grooves which are in some cases narrow and wavy at their edges. This suggests that the four small unsteady vortices are responsible for the enhancement and the transient character of the attenuation of the laser beam reaching the target surface. This can be explained by particles trapping in the vortex cores where the pressure is lesser so that they stay a longer time near the target surface. This scenario is consistent with the increase in the average sizes of the particles observed in regime C. Likewise, another explanation for the role of the small unsteady vortices in the laser beam attenuation could be the trapping of bubbles in the vortices cores. Microbubbles are formed during the ablation process18 and migrate in the solution under the combined effect of buoyancy forces and fluid flow. There are several

theoretical and experimental evidences[25,26] that these bubbles can also accumulate in low pressure zones corresponding to the vortices cores.

A further interesting result was the size distribution of the produced particles and the fact the particles are mainly spherical with no evidence of fusion and aggregation. Usually such small particles can only be generated by PLAL using surfactants[14]. The main characteristics of the produced NPs (size, shape, purity) are very suitable for catalysis and other applications involving charge transfer and/or surface functionalization.[27,28]

The generation of so small Ag nanoparticles *in pure water* by PLAL has rarely been reported. Pyatenko et al. [29] obtained a similar size distribution to that presented in Fig.3 (c) using, as in this work, a tightly focused beam and a repetition rate of 10 Hz but with much higher energy (320 mJ/pulse) and different wavelength (532 nm) . As assumed by these authors in their study, it is also likely that our generated particles are primary particles. The latter correspond to particles formed at the earlier stage of the process via coalescence mechanisms in the laser induced cavitation bubble. Their size distribution is log-normal with a large tail to the right in good agreement with coalescence[30]as expected for their formation mechanism in the cavitation bubble[31,32,33,34]. Furthermore, these as-formed particles are quickly carried in the bulk solution by the flow preventing i) local accumulation of the particles in front of the target and their aggregation/coalescence[3] and ii) their interaction with subsequent laser pulses and fragmentation[16]. Even at the lowest rotation rate, the flow velocity of the liquid near the target is about 10^{-1} $m.s^{-1}$ (Fig. 7(a)) which means that during the pulses (0.1 s) the particles carried by the flow almost travel 1 cm.

It should also be noted that we used a focusing lens with low f/# (f/4). In such focusing conditions, the laser fluence decreases rapidly as the distance from the target increases because of its inverse dependence on the diameter squared. The particles fragmentation may occur in the region of the beam where the fluence is sufficiently high to provoke their

vaporisation otherwise they can only be, in the best case, reshaped via melting[15]. Additionally, to have a significant impact on the size distribution, the interaction volume with fluence above the vaporization threshold must be not too small compared to the total volume of the solution otherwise longer experiment duration is required[35]. The fluence threshold for the vaporisation/fragmentation of particles with size in the range of tens nm is estimated from Ref. 15 to be 2 J/cm^2. Due to the convergence of the laser beam, the irradiated volume above this fluence threshold is of the order of 2×10^{-3} cm^3 which is four order magnitudes lower than the total volume of the solution (20 cm^3).

Furthermore, the volume-weighted size distribution (Fig. 3(e, f)) revealed that the observed average size of the primary particles is similar to that estimated from in situ study using small angle X-ray scattering[31,32,33] (SAXS) carried out with laser parameters close to ours. This is explained by the fact that SAXS is more sensitive to volume (or mass) rather than particle number[31,32,33].

For all these reasons, it is much more likely that the generated particles are primary particles rather than fragmentation products.

Using theoretical calculations based on shape distributed effective medium theory (SDEMT)[Erreur ! Signet non défini.], the volume fraction of the obtained particles was estimated to be about 10^{-4} % (with an relative uncertainty of about 10 %) which corresponds to an ablation rate of about 1.2 mg/h which corresponds to a relative productivity of about 3.6 mg/Wh. The production yield can be further improved by increasing the repetition rate of the laser[19,36]. To this end, the fact that the repeatability of the process is conserved in regime B (up to about 1500 rpm, Fig. 3(a)) should enable the conduction of the process with much higher repetition rate. Commercially available Nd-YAG laser sources can display repetition rates of several hundreds of Hz offering the possibility to increase the production yield by one order of magnitude. Further increasing by another order of magnitude the repetition rate (in the kHz

range) would raise the issue of the interaction of the laser beam with the cavitation bubbles[18]. In laser conditions close to those of this work, the cavitation bubble generated, after a laser pulse, can reach a radius of about 1 mm in 150-200 μs[34]. At high repetition rate, the interaction of the laser pulse with the bubble generated by the previous laser pulse can scatter, absorb or reflect this laser beam reducing the ablation rate. Therefore, the distance between two consecutive laser impacts on the target must exceed the maximum bubble diameter. At 1500 rpm, the maximum repetition rate of the laser that fulfills this condition has been calculated to be about 4 kHz which would in theory increases by a factor 400 the productivity.

Conclusions

In summary, PLAL with a high-speed rotation target enables the generation of very small particles *in pure water* that are very likely to be primary particles. When tuning the rotation rate of the target, the calculated flow patterns reveal different hydrodynamic regimes which are correlated to the repeatability and the ablation rate of the process. The use of this system at higher laser repetition rate (kHz range) would *in principle* enables the *repeatable* production of high-purity nanoparticles showing average size of 3.3 nm. However, another problem raised by the increase of the repetition rate is the accumulation of the generated particles in front of the target. At 4 kHz, it is not clear whether the particles transport in the bulk solution would be sufficiently rapid to prevent this problem. This last point requires further investigations on the combined effects of repetition rate of the laser and rotation rate of the target and experiment with longer ablation time.

Acknowledgements

N.C. wishes to thank Pr. Stephan Barcikowski for helpful discussions.

References

[1] A. Fojtik and A. Henglein, *Ber. Bunsen-Ges. Phys. Chem.*, 1993, **97**, 252.

[2] V. Amendola and M. Meneghetti, *Phys. Chem. Chem. Phys.*, 2009, **11**, 3805.

[3] V. Amendola and M. Meneghetti, *Phys. Chem. Chem. Phys.*, 2013, **15**, 3027.

[4] S. Barcikowski and G. Compagnini, *Phys. Chem. Chem. Phys.*, 2013, **15**, 3022.

[5] E. Boisselier and D. Astruc, *Chem. Soc. Rev.*, 2009, **38**, 1759.

[6] E.C. Dreaden, A.M. Alkilany, X. Huang, C.J. Murphy and M.A. El-Sayed, *Chem. Soc. Rev.*, 2012, **41**, 2740.

[7] F. Frederix, J. M. Friedt, K. H. Choi, W. Laureyn, A. Campitelli, D. Mondelears, G. Maes and G. Borghs, *Anal. Chem.*, 2003, **75**, 6894.

[8] M. M. Harper, K. S. McKeating and K. Faulds, *Phys. Chem. Chem. Phys.*, 2013, **15**, 5312.

[9] P. Liu, Y. Liang, X. Lin, C. X. Wang and G. Yang, *ACS Nano*, 2011, **5**, 4748.

[10] M. Lau, A. Ziefuss, T. Komossa and S. Barcikowski, *Phys. Chem. Chem. Phys.*, 2015, **17**, 29311.

[11] G. Compagnini, E. Messina, R.S. Cataliotti, A. Grillo and G. Giaquinta, *Phil. Mag. Lett.*, 2009, **89**, 250.

[12] T. Tsuji, K. Iryo, N. Watanabe, M. Tsuji, *Appl. Surf. Sco. A*, 2002, **202**, 80.

[13] M. Prochazka, P. Mojzes, J. Stepanek, B. Vickova and P. Turpin, *Anal. Chem.*, 1997, **69**, 5103.

[14] F. Mafune, J. Kohno, Y. Tadeka, T. Kondow and H. Sawabe, *J. Phys. Chem. B*, 2000, **104**, 9111.

[15] A. Resano-Garcia, Y. Battie, A. Koch, A. En Naciri and N. Chaoui, *Nanotechnology*, 2016, **27**, 215705

[16] T. Tsuji, K. Iryo, Y. Nishimura, M. Tsuji, *J. Photochem. Photobiol. A*, 2001, **145**, 201.

[17] A. Resano-Garcia, Y. Battie, A. Koch, A. En Naciri and N. Chaoui, *J. Appl. Phys.*, 2015, **117**, 113103.

[18] S. Barcikowski, A. Menéndez-Manjón, B. Chichkov, M. Brikas and G. Račiukaitis, *Appl. Phys Lett.*, 2007, **91,** 083113.

[19] R. Steubel, G. Bendt and B. Gökce, *Nanotechnology*, 2016, 27, 205602

[20] D.R. Gabe and F.C. Walsh, *J. Appl. Electrochem.*, 1983, 13, 3.

[21] R. De Loor, Phys. Proc., 2013, **41**, 544.

[22] G. Marzun, J. Nakamura, X. Zhang, S. Barcikowski and P. Wagener, *Appl. Surf. Sci.*, 2015 **348,** 75.

[23] M. F. A. Couette, Études sur le frottement des liquides, (Gauthier-Villars, Paris, 1890).

[24] T. von Kármán, *Zeit Angew. Math. Mech.* , 1921, **1**, 233.

[25] E. Climent, M. Simmonet and J. Magnaudet, *Phys. Fluids*, 2007, **19**, 083301.

[26] Y. Murai, H. Oiwa and Y. Takeda, *Phys. Fluids*, 2008, **20**, 034101.

[27] J. Zhang, M. Chaker and D. Ma, *J. Colloid Interf. Sci.*, 2016, in press

[28] D. Wodka, E. Bielanska, R.P. Socha, M. Elzbiecak-Wodka, J. Gurgul, P. Nowak, P. Warszynski and I. Kumakiri, *ACS Appl. Mat. Interf.*, **2** (2010) 1945.

[29] A. Pyatenko, K. Shimokawa, M. Yamagushi, O. Nishimura and M. Suzuki *Appl. Phys. A*, 2004, **79**, 803.

[30] C. G. Granqvist and R.A. Buhrman, *J. Appl. Phys.*, 1976, **47**, 2200.

[31] P. Wagener, S. Ibrahimkutty, A. Menzel, A. Plech and S. Barcikowski, *Appl. Phys. Lett.*, 2012, **101**, 103104.

[32] P. Wagener, S. Ibrahimkutty, A. Menzel, A. Plech and S. Barcikowski, *Phys. Chem. Chem. Phys.*, 2013, **15**, 1568.

[33] S. Ibrahimkutty, P. Wagener, T. dos Santos Rolo, D. Karpov, A. Menzel, T. Baumbach, S. Barcikowski and A. Plech, *Sci. Rep.*, 2015, **5**, 16313.

[34] J. Lam, J. Lombard, C. Dujardin, G. Ledoux , S. Merabia and D. Amans, *Appl. Phys. Lett.*, 2016, **108**, 074104.

[35] A.V. Simakin, V.V. Voronov, N.A. Kirichenko and G.A. Shafeev, *Appl. Phys. A*, 2004, **79**, 1127.

[36] G. Messina, P.Wagener, R. Steubel, A. De Giacomo, A. Santagata, G. Compagnini and S. Barcikowski, *Phys. Chem. Chem. Phys.*, 2013, **15**, 3093.